Article

Ligand-dependent energetics for dehydrogenation: Implications in Li-ion battery electrolyte stability and selective oxidation catalysis of hydrogen-containing molecules

Livia Giordano, Thomas M. Østergaard, Sokseiha Muy, Yang Yu, Nenian Charles, Soo Kim, Yirui Zhang, Filippo Maglia, Roland Jung, Isaac Lund, Jan Rossmeisl, and Yang Shao-Horn

Chem. Mater., **Just Accepted Manuscript** • DOI: 10.1021/acs.chemmater.9b00767 • Publication Date (Web): 03 Jul 2019

Ligand-dependent energetics for dehydrogenation: Implications in Li-ion battery electrolyte stability and selective oxidation catalysis of hydrogen-containing molecules.

Livia Giordano,[a,b]* Thomas M. Østergaard,[d] Sokseiha Muy,[a] Yang Yu,[c] Nenian Charles,[a] Soo Kim,[a] Yirui Zhang,[b] Filippo Maglia,[e] Roland Jung,[e] Isaac Lund,[f] Jan Rossmeisl,[d] Yang Shao-Horn[b,c]*

[a]Research Laboratory of Electronics, [b]Department of Mechanical Engineering, [c]Department of Materials Science & Engineering, Massachusetts Institute of Technology, 77 Massachusetts Avenue, Cambridge, MA, 02139, USA

[d]Nano-Science Center, Department of Chemistry, University of Copenhagen, DK-2100 Copenhagen, Denmark

[e]BMW Group, Petuelring 130, 80788 München, Germany

[f]BMW Group Technology Office USA, 2606 Bayshore Parkway, Mountain View, California 94043, United States

ABSTRACT: The hydrogen adsorption energetics on the surface of inorganic compounds can be used to predict electrolyte stability in Li-ion batteries and catalytic activity for selective oxidation of small molecules such as H_2 and CH_4. Using first-principles density functional theory (DFT), the hydrogen adsorption was found to be unfavorable on high band-gap insulators, which could be attributed to lower energy level associated with adsorbed hydrogen relative to the bottom of conduction band. In contrast, the hydrogen adsorption was shown the most favorable on metallic and semiconducting compounds, which results from an electron transfer from adsorbed hydrogen to the Fermi level or the bottom of conduction band. Of significance, computed hydrogen adsorption energetics on insulating, semiconducting and metallic oxides, phosphates, fluorides, and sulfides were decreased by lowering the ligand *p* band center while the energy penalty for ligand vacancy formation was increased, indicative of decreased surface reducibility. A statistical regression analysis, where 16 structural and electronic parameters such as metal-ligand distance, electronegativity difference, Bader charges, bulk and surface metal and ligand band centers, band gap, ligand band width and work function were examined, further showed that the surface ligand *p* band center is the most accurate single descriptor that governs the hydrogen adsorption tendency, and additional considerations of the band gap and average metal-ligand distance further reconcile the differences among compounds with different ligands/structures, which ligand bands are different in shape and width. We discuss the implications of these findings for passivating coatings and catalysts design and the need for novel theoretical methods to accurately estimate these quantities from first principles. These results establish a universal design principle for future high-throughput studies aiming to design electrode surfaces to minimize electrolyte oxidation by dehydrogenation in Li-ion batteries and enhance the H-H and C-H activation for selective oxidation catalysis.

INTRODUCTION

Inorganic compounds with transition metals including metal oxides,[1,2] phosphates,[3,4] fluorides,[5] and sulfides[6,7] are used in energy applications such as Li-ion batteries, [8,9,10,11] water splitting[12,13,14] and (electro)catalysis of hydrogenation/dehydrogenation.[15,16,17] Generally speaking, the reduction/oxidation (redox) of transition metal ions (or centers) governs the lithium intercalation voltage and capacity.[18] Lowering the energy of transition metal density of states (DOS) increases lithium intercalation voltage,[19] which can be further tuned by changing the crystal structures[20,21,19] and/or the nature of metal-ligands.[22,23] Similarly, the redox of transition metal ions can greatly influence surface adsorption energetics,[24,25] which is critical to control catalytic activity (using the Sabatier principle: not too strong nor too weak absorption of reaction intermediates to maximize activity)[26,27] and selectivity.[28] Recent work has shown that activating ligand redox by tuning the nature of metal-ligand bonds,[29,30,31,32,33] can greatly influence the stability of lithium battery electrodes[34,35,36,37] and electrolytes,[38,39,40,41] potentially enhance lithium intercalation capacity[30,42] through increasing the electrons stored not only on transition metal ions and but also oxygen ions, [43,44,45] and promote the kinetics of oxidation

reactions,[46,47,48] which represent great opportunities for the design of new Li-ion storage materials, and oxidation catalysts.

The redox of ligands can be activated by increasing the contribution of ligand DOS near the Fermi level, where ligand/anion redox in addition to metal redox can occur in solids.[32,29] For example, strong metal-oxygen hybridization can lead to the formation of ligand holes in late transition metal oxides,[49,50] and the redox of ligand nonbonding states[19] can generate new anion clusters in metal selenides,[32] sulfides[51,52] and oxides[31,53]. Using more electronegative metals can lower the energy of antibonding states (largely metal character[19,29,54]) while having less electronegative ligands can increase the energy of bonding states (largely ligand character[32]), both of which can lead to increased density of states from the ligand near the Fermi level.[19] When the Fermi level is lowered into the O(2p) states upon lithium de-intercalation from late transition metal oxides during charging of Li-ion batteries, these oxides become unstable against oxygen evolution, as oxide ions can be oxidized to molecular oxygen to form spinel or rocksalt as observed on $Li_xNi_{0.8}Co_{0.2}O_2$,[55] $Li_xNi_{1/3}Mn_{1/3}Co_{1/3}O_2$,[56] $Li_xNi_{0.4}Mn_{0.4}Co_{0.18}Ti_{0.02}O_2$[57], and $Li_xNi_{0.8}Co_{0.15}Al_{0.05}O_2$[58]. Evolution of highly reactive singlet oxygen has also been reported, which can readily attack the electrolyte.[59,60] In addition, oxidation of anions or oxide ions has been attributed to additional capacities to metal redox in Li-rich layered materials (*e.g.* Li_2RuO_3,[30] Li_2IrO_3,[61] and $Li_{1.2}Ti_{0.4}Mn_{0.4}O_2$[62]) and cation disordered layered oxides such as $Li_2Mn_{2/3}Nb_{1/3}O_2F$[63]and Li_2MnO_2F.[64] Moreover, the redox or activation of oxygen sites for highly covalent oxides such as $SrCoO_3$[46,65] can promote the kinetics of oxygen evolution reaction (OER) upon water electrochemical oxidation in addition to transition metal sites. [66,2,27] Furthermore, the activation of oxygen sites of high-capacity Li-ion electrode materials such as $LiNi_xCo_yMn_{1-x-y}O_2$ (NMC) can promote the dehydrogenation of carbonate-based electrolytes[67], which is enhanced with moving the Fermi level closer to the O 2p band center associated with increasing Ni and/or decreasing lithium content.[41,68,67] Specifically, electrolyte solvents like ethylene carbonate (EC) can be energetically favorable to dissociate at a C-H bond and adsorb the two fragments on surface oxygen sites,[41,69,70] where the reduction of two transition metal ions accompanies the electron displacements induced by the newly formed C-O and O-H bonds upon dissociative adsorption (Figure 1a[41,68]). This process is more favorable than electrophilic attack,[71,72] nucleophilic attack,[73] dissociation with the formation of an oxygen vacancy[71] and ring opening[74,72]. The dissociative adsorption energetics of C-H bonds on surface oxygen sites correlates with hydrogen adsorption energy such as $\frac{1}{2}\ H_2 + O{-}M^{n+}{-}O \rightarrow *H^+ + O{-}M^{(n-1)+}{-}O$ (Figure 1b) for Li_xMO_2 layered oxides.[68] This process can be considered analogous to the C-H activation of methane or other small hydrocarbons on oxides via oxidative adsorption at the oxygen sites (Figure 1c) as reported for perovskite oxides [47], transition-metal-doped La_2O_3[75] and CeO_2[76,77]. We note that on high band gap materials this homolytic dissociation becomes energetically unfavorable and the H-H and C-H bond dissociation occurs heterolytically at the metal and oxygen site.[78,79] Similarly to the EC dissociation, the small hydrocarbons C-H activation has been correlated with the hydrogen adsorption energy[47,80] and oxide reducibility[48,77], where on the surface of ABO_3 perovskites, the activation barrier for methane first C-H dissociation correlates with the hydrogen adsorption energy (Figure 1e[47]). Late 3*d* transition metal perovskites are more active compared to early transition metals, while the A site has a lesser effect on the oxygen activity (Figure 1e).[47] Therefore, hydrogen adsorption energetics on surfaces can be used to measure the thermodynamic driving force for dehydrogenation of aprotic electrolytes in Li-Ion batteries, and the kinetics of hydrogen oxidation and selective oxidation of hydrocarbons.

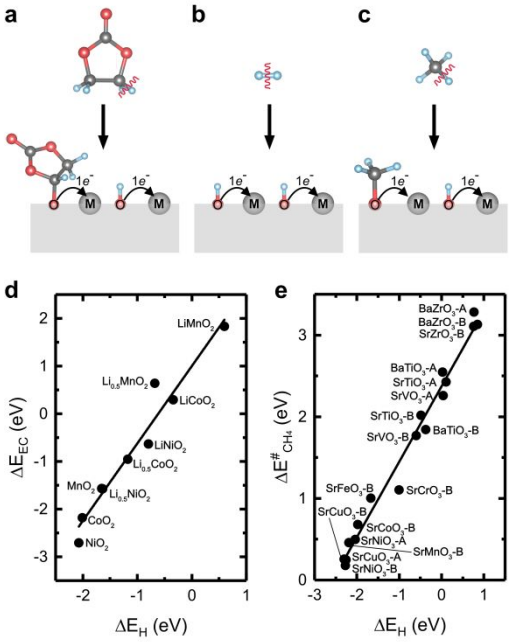

Figure 1. Analogy between ethylene carbonate (EC) dissociative adsorption, hydrogen adsorption and methane C-H activation on transition metal oxides, involving the reduction of the oxide transition metal ions on reducible oxides, $C_xO_yH_z + 2\ O{-}M^{n+}{-}O \rightarrow *C_xO_yH_{z-1}{}^+ + *H^+ + 2\ O{-}M^{(n-1)+}{-}O$, where $*C_xO_yH_{z-1}$ and *H represent the molecule ($C_xO_yH_z$) decomposition products adsorbed on the surface of the oxides (O−M−O). (a-c) Schematic representation of EC, H_2 and CH_4 dissociative adsorption highlighting the interfacial electron transfer. (d) Adsorption energy for EC dissociative adsorption (ΔE_{EC}) as a function of hydrogen adsorption energy (ΔE_H) on the $(10\bar{1}4)$ surface of Li_xMO_2 layered compounds (M = Mn, Co and Ni; x=1, 0.5, 0) as reported in previous work[68], computed at PBE level of theory. (e) Activation energy for CH_4 dissociative adsorption ($\Delta E^{\#}_{CH4}$) as a function of hydrogen adsorption (ΔE_H) on the A- or B- terminated (001) surface of perovskite ABO_3 oxides (A = Sr and Ba, B = Ti, V, Cr, Mn, Fe, Co, Ni, Cu, and Zr) as reported in Ref. 47, computed at PBE level of theory with D3 van der Waals correction. Note that the hydrogen reference has been changed from atomic H to 1/2 H_2 molecule compared to previous work[47].

Here we examine the hydrogen adsorption energy on a library of inorganic compounds beyond oxides, which can used as a direct measure or activity descriptor for the selective oxidation of molecules such as hydrogen and C-H bond containing molecules. We study the hydrogen adsorption and anion vacancy formation energy on a variety of ionic compounds, including oxides, phosphates, fluorides and

sulfides, with the aim of understanding the physical properties governing surface activity, and anion activation or release. We have used a data-driven statistical analysis to identify descriptors for hydrogen adsorption, with increased predictive power. We have included in the analysis physical and chemical properties of materials bulk and surface, such as metal-ligand distance, electronegativity difference, Bader charges, bulk and surface metal/ligand band centers, band gap, ligand band width and work function. We have demonstrated that beyond the oxygen *p* band previously reported, a combination of features, including structural (metal-ligand distances) and electronic properties (band gap), are required to fully capture the hydrogen adsorption energy of the diverse classes of materials reported here. These results can be used to accelerate the design and optimization of high-performant and stable materials for energy applications or coatings to prevent degradation phenomena.

COMPUTATIONAL METHODS

Periodic plane wave Density Functional Theory (DFT) calculations were performed to study the hydrogen adsorption and ligand vacancy formation energy on a number of oxides, fluorides, sulfites and phosphate surfaces. We used the PBE functional[81] as implemented in the Vienna Ab Initio Simulation Package (VASP) code, [82,83] and Projector Augmented Wave (PAW) for the description of the core-electron interaction, and the plane wave cutoff was set to 450 eV. The PBE functional was chosen to have a consistent method among the materials studied. Although DFT+U[84,85] or hybrid functionals[86,87] would be more appropriate for the study of electron localization in correlated materials, they rely on material-dependent empirical parameters (U value[88],[89] and percentage of HF exchange[90]), making difficult to apply them for screening a large scope of materials. We note that similar trend was found for EC dissociation versus the O(2*p*) band at PBE+U[41] and PBE[68] level, validating the use of PBE for this quantity. We are aware that other physical properties are not well reproduced at PBE level, i.e. the gap band is notoriously underestimated, so that not the absolute values but rather the trends are discussed in relation to these features. The surfaces were modeled with slabs of least four-layer thick (Table S1), separated by at least 13 Å and a dipole correction was applied in order to eliminate spurious interactions across the periodic boundary along the direction perpendicular to the surface. About 25% of the slab, closest to the surface, and the adsorbate atomic positions were allowed to fully relax. Hydrogen was adsorbed on one side of the slab only. To avoid lateral interactions between adsorbates, surface supercells of surface area between 25 and 36 Å^2 were used, and a single H atom was adsorbed per unit cell. Additional details on the surface models, including surface unit cells and number of layers, can be found in Table S1. All calculations were spin-polarized, where a ferromagnetic order was assumed for all magnetic compounds, except for MF_2 and MO rocksalt compounds where an antiferromagnetic order was considered. The Bader decomposition method was used for the estimation of charge transfer.[91,92] For each class of materials we choose the most representative space group for the simulations and we built the surface models for the most stable surface orientation reported in the literature from previous computational studies (Table S1).

A statistical regression analysis was used to develop quantitative structure-property relationships (QSPRs) for the hydrogen adsorption energy. We identified 38 features (or descriptors), issued from the bulk and surface physico-chemical properties, which include structural features (d(M-L) distance), and electronic properties (charges, electronic band centers, band width, band gap and work function). For the electronic band centers, several features where identified for each band, depending on the integration range (i.e. all range or filled/empty states only) and the energy reference for semiconductors and insulators (valence band maximum, mid-gap or conduction band minimum), Figure S1. As some of the bulk and surface descriptors where found to be highly correlated ($r^2 > 0.80$), we identified a subset of 28 descriptors for the single coefficient regression analysis, 16 of those being primary features and the other 12 secondary features, which can be derived from primary features with simple algebra. The 16 primary features where used for the multiple variable regression analysis.

The predictive power of the different regression methods was compared by randomly dividing the 51 adsorption energy data in a training set (80% of data set) and a test set (20% of data set). The data were standardized to correct for the different scale of the features, by using the mean and standard deviation of the training set. The training set was used to fit the model, and a 5-fold cross-validation was used to determine the optimal fitting coefficients for the regularized regressions. The out-of-bag error was used to select the optimal parameters for the number of trees and the maximum depth of trees in the random forest. Other parameters was set to the default values as implemented in the scikit-learn package.[93] The accuracy of the different QSPRs was assessed by comparing the mean absolute error (MAE) on the test set. Linear regression, Random Forest and regularized methods, namely least absolute shrinkage and selection operator (LASSO), Ridge and Elastic Net regression, as implemented in scikit-learn[93] were used to determine the QSPRs.

RESULTS AND DISCUSSION

We first show that the ligand *p* band descriptor for hydrogen adsorption energy can be generalized to a wide range of crystal families and ligands. Figure 2 shows some of the surfaces used in the material screening, which include $LiMO_2$ layered oxides and sulfites, MO rock-salt oxides, rutile oxides and fluorides, phosphates and other binary and ternary oxides (see Table S1 for a complete list). The surface orientations were chosen as the most stable reported in the literature from previous computational studies, Figure 2 and Table S1. The hydrogen adsorption energy, ΔE_H, has been computed with respect to H_2 in the gas phase: $\Delta E_H = E(*H) - ½ E(H_2) - E(*)$, where $E(*H)$, $E(H_2)$, and $E(*)$ are the DFT total energies of hydrogen adsorbed on the surface (*H), H_2 in the gas phase (H_2), and of the bare surface (*), respectively. A negative binding energy is indicative of an exothermic hydrogen adsorption. Hydrogen atom was found to preferentially adsorb on the anion site for all the materials considered.[94,95] The desired hydrogen adsorption energy depends on the specific application. In Li-ion batteries, the electrode surface or the coating material should have low affinity for hydrogen, and thus a positive hydrogen binding energy, in order to prevent the formation of acidic OH groups which can attack the electrolyte salt anions.[96,97,67] In catalysis and electrocatalysis an intermediate hydrogen binding energy is preferable, so that the reaction intermediates bound to the surface neither to strongly or too weakly.[26,27]

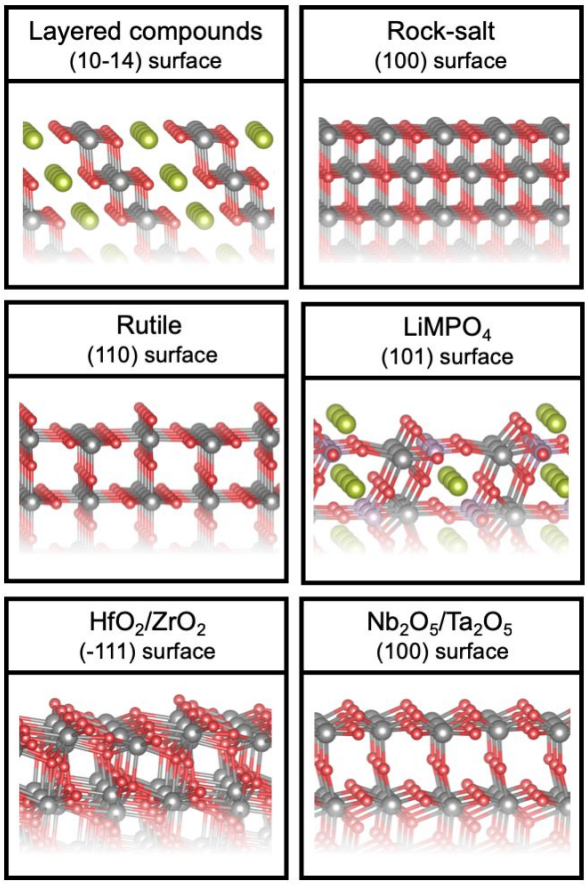

Figure 2. Surface models of representative oxides, fluorides, sulfites and phosphates used to compute the hydrogen adsorption and the ligand vacancy formation in this work. Oxygen is represented in red, lithium in green, metals in gray, phosphorous in light purple. A complete list of space groups and surface orientations is reported in Table S1.

The bulk oxygen 2*p* band center was found to correlate with the adsorption energy of dissociated EC[41,68] and with the oxygen vacancy formation energy in oxides for oxygen electrocatalysis.[98] It is thus interesting to see if this descriptor is able to capture the thermodynamics of hydrogen adsorption over the large chemical space spanned here. The hydrogen adsorption energy on the materials studied in this work is reported in Figure 3 as a function of the bulk ligand *p* band center. A clear trend can be seen in Figure 3a, where the materials with ligand *p* band higher in energy are the more prone to react with hydrogen. Moreover, metallic and low band gap semiconductors have a higher tendency to bind hydrogen than materials with larger band gap. This is due to the different tendency of these substrates to be reduced and results in a different nature of the adsorbate. In case of high band gap compounds, the electron transfer to the substrate is not favorable and hydrogen is physisorbed in a neutral form (Figure 3b and 4c). This is the case of LiF, MnF_2 and SiO_2, where the adsorption energy approaches 2.2 eV with respect to ½ H_2, which corresponds to zero binding energy with respect to the hydrogen atom, and can thus been considered as an upper limit for ΔE_H. We note that in this case, other adsorption modes, such has undissociative adsorption or heterolytic dissociation (or formation of Lewis acid-base pairs) becomes more favorable.[78,99] Low band gap semiconductors instead get reduced when H is adsorbed, and one electron is transferred from hydrogen to the bottom of the conduction band, usually formed by metal *d* band states (Figure 3c and 4b), or to a localized polaron, giving rise to gap states close to the conduction band.[94] Finally, in metallic compounds the adsorbed hydrogen transfers its electron to the Fermi level, usually with transition metal *d* states parentage (Figure 3d and 4a).

Comparing the material families, our results indicate that fluorides and phosphates have a lower tendency to bind with hydrogen compared to oxides. We also note that for similar values of ligand *p* band, sulfites have a lower tendency to adsorb hydrogen, which results in a slightly positive binding energy, compared to the negative binding energy of the oxides with comparable ligand *p* band center. This can be attributed to the weaker S-H bond, compared to O-H, as demonstrated by the larger enthalpy of formation of gas phase H_2O (-242 kJ/mol[100]) compared to H_2S (-21 kJ/mol[100]) and the larger L-H distance (O-H ≈ 1 Å and S-H ≈ 1.2 Å). Conversely, despite the stronger L-H bond (HF enthalpy of formation of -273 kJ/mol[100] and F-H distance around 0.9 Å) fluorides have comparable binding energy as semiconducting oxides but lower ligand *p* bands, due the higher electronegativity of fluorine, which also corresponds to a weaker L-M overlap and smaller band width of fluorides (Figure S2). Finally, phosphates have binding energy close to oxides with the same ligand *p* band, which is not surprising as the valence band of phosphates is dominated by the oxygen states.

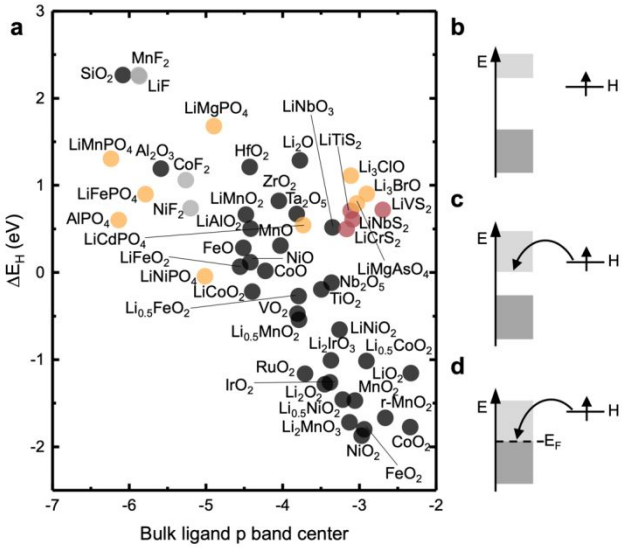

Figure 3. (a) Hydrogen adsorption energy with respect to the bulk ligand *p* band center, referred to the Fermi level for metals and mid-gap for semiconductors and insulators. Oxides are represented in black, fluorides in gray, sulfides in red, phosphates, arsenates and inverse perovskites in orange. (b-d) Schematic representation of the charge transfer between adsorbed hydrogen and surfaces with different electronic structures: (b) high band gap insulators, (c) semiconductors and (d) metals.

The different nature of adsorbed hydrogen is more clearly illustrated by the Density of States (DOS) reported in Figure 4. When hydrogen is adsorbed on RuO_2, a metallic oxide, it forms a bond with a surface oxygen, resulting in the appearance of a bonding state in the DOS at ~ -8 eV (Figure 4a, bottom panel), while one electron is transferred to the Fermi level, without changing the oxide DOS significantly. On the other hand, in the case of semiconducting TiO_2 the oxide DOS is highly altered by the adsorption of hydrogen. In absence of hydrogen, the valence band is completely filled and the conduction band is empty. On the contrary, when H is adsorbed, the Fermi level is displaced into the conduction band, indicating that the oxide is partially reduced (Figure 4b). Finally, the large band gap of Al_2O_3 prevents the charge transfer to the bottom of the conduction band, and the electron displaced by the formation of the OH bond creates a localized state in the band gap of the oxide. In the case of Al_2O_3(0001) reported in Figure 4c, the electron is localized on the undercoordinated Al atom on the oxide surface.

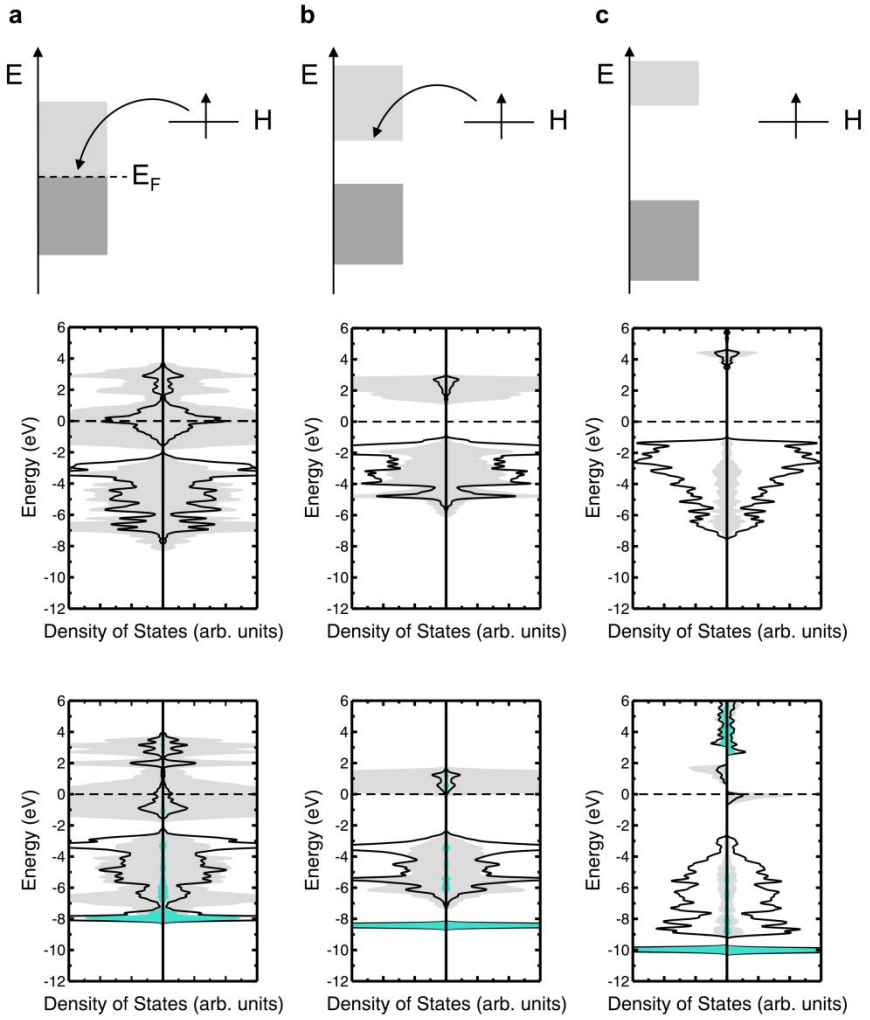

Figure 4. Top: Top: schematic representation of the charge transfer between adsorbed hydrogen and the surface for materials with different band gap: (a) metallic, (b) semiconducting and (c) high band gap insulating compounds. The Density of States for the surfaces of corresponding materials: (a) metallic RuO_2, (b) semiconducting TiO_2 and (c) high band gap insulating Al_2O_3, are shown without (middle panels) and with (bottom panels) adsorbed hydrogen. Projected DOS on the surface oxygen where hydrogen is adsorbed, on neighbor metal atoms and on hydrogen are reported in black, gray and light blue, respectively. We note that in the case of TiO_2 the electron is delocalized on the conduction band at the PBE level used here, while it would be localized on a Ti^{3+} polaron at PBE+U or hybrid functional level.[94]

The surface ligand vacancy formation energy follows a similar trend with the bulk ligand *p* band center (Figure 5a), confirming what already reported for oxide perovskites-based oxygen electrocatalysts.[98] As a consequence of the similar correlation with the ligand *p* band center, we found a linear trend between the hydrogen adsorption energy and the surface ligand vacancy formation energy, as reported in Figure 5b. Notably, we observe a better correlation for hydrogen adsorption energy and surface ligand vacancy formation energy compared to the correlation of these two properties with the *p* band center, probably because of the error introduced by comparing a bulk property (ligand *p* band center) with a surface property such as the hydrogen adsorption energy or the surface ligand vacancy formation

energy. Indeed, a better correlation of the hydrogen adsorption energy with the surface O(2*p*) band was observed in Ref. 68. The correlation between the hydrogen adsorption energy and oxygen vacancy formation energy has been already reported for oxide catalysts for hydrocarbons C-H activation,[47,48,101,77] but it is remarkable that it holds on the wide range of materials studied in this work. Moreover, the trends reported in Figure 5 indicate that the surface reactivity and the tendency to release oxygen scale together, as observed on Ni-rich NMC positive electrodes for Li-ion batteries, where both the onset potential for oxygen release is lowered and the surface reactivity is greatly enhanced for Ni-rich materials.[67,35]

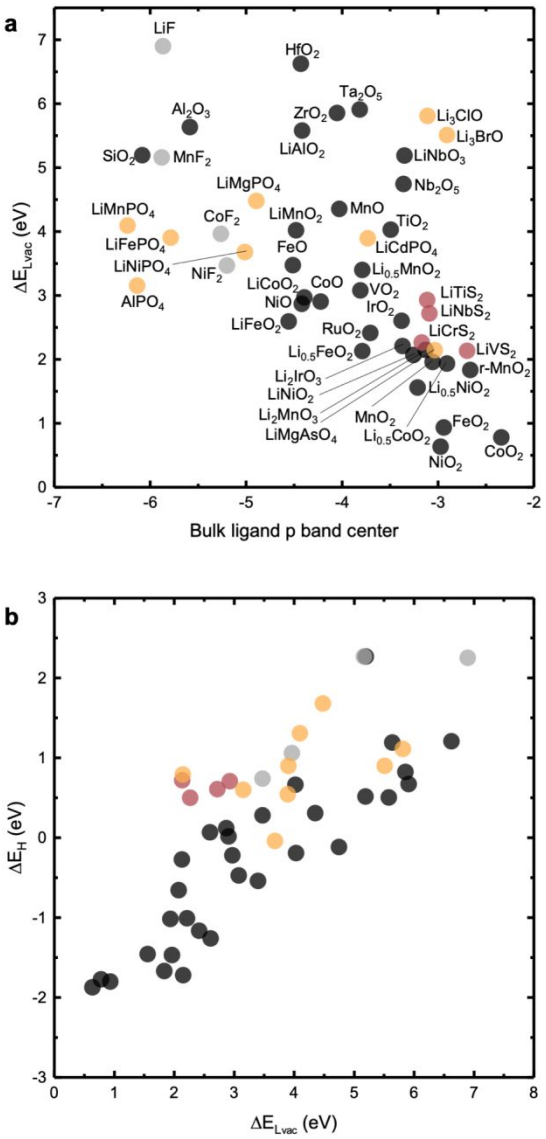

Figure 5. (a) Surface ligand vacancy formation energy with respect to the bulk ligand *p* band center, referred to the Fermi level for metals and mid-gap for semiconductors and insulators. (b) Hydrogen adsorption energy as a function of surface ligand vacancy formation energy. Oxides are represented in black, fluorides in gray, sulfides in red, phosphates, arsenates and inverse perovskites in orange.

In the previous discussion we have considered the dependence of the hydrogen adsorption energy on the bulk ligand *p* band center. However, questions arise on whether there are other fundamental properties of the material (descriptors or features) that better correlate with the hydrogen adsorption energy and whether a single descriptor can capture this property on the chemical space we have explored. In order to answer these questions, we have performed a single-feature linear regression analysis of the hydrogen adsorption energy with respect to a number of material properties, which are reported in Table 1. We have included properties of bulk material, adsorbate-free surface and surface with adsorbed hydrogen. As bulk properties we have considered the bulk M-L distance, metal and ligand Bader charges, ligand and metal band centers, ligand band width, band gap, and average bond iconicity. We have then considered the corresponding surface properties, such as the ligand and metal band center, surface band gap and work function, as well as the work function of the system with adsorbed hydrogen. We also included some secondary features, derived from the primary features reported in Table 1. In particular, the DOS issued from the calculations are typically referred to the highest occupied states, *i.e.* the top of the valence band for materials with a band gap. We also considered the DOS-related features referred to half-gap or to the bottom of the conduction band (conduction band minimum, CBM), as secondary features. Specifically, the secondary features encompass charge transfer gap (CT = (M(d)-e)-(L(p)-f)), band centers referred to mid-gap or the conduction band minimum (i. e. L(p)* = L(p) – ½ Gap; L(p)** = L(p) -Gap), work function referenced to the conduction band minimum, corresponding to the position of CBM with respect to vacuum (WF** = WF-(Gap-surf)), and work function difference (dWF = (WF-H) – WF). Additional surface properties, such as surface ligand and metal distances and charges or empty and filled surface band centers, do not bring new information as strongly correlated with the respective bulk properties (R^2 > 0.80), Figure S3, and are thus not included in the analysis.

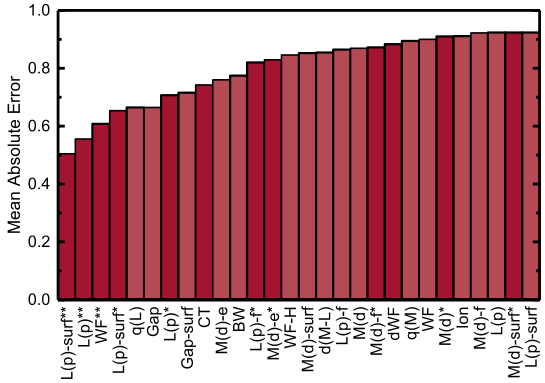

Figure 6. Mean absolute error for single descriptors of computed hydrogen adsorption energy, which include average bulk M-L distance (d(M-L)), metal and ligand Bader charges (q(M) and q(L)), ligand p band center referenced to VBM, mid-gap or CBM (L(p), L(p)*, L(p)**), filled states ligand *p* band center referenced to VBM or mid-gap (L(p)-f and L(p)-f*), metal *d* band center referenced to VBM or mid-gap (M(d) and M(d)*), filled and empty states metal *d* band center referenced to VBM or mid-gap (M(d)-f, M(d)-f*, M(d)-e and M(d)-e*), charge transfer energy (CT), bulk DFT band gap (Gap), ligand band width (BW), ionicity (Ion), surface ligand *p* band center referenced to VBM, mid-gap or CBM (L(p)-surf, L(p)-surf* and L(p)-surf**), surface band gap (Gap-surf), work function (WF), work function (WF) referenced to the CBM (WF**), work function of surface with

adsorbed hydrogen (WF-H) and work function difference (dWF). All data are included in the analysis. The descriptors are reported in order of significance, from the most to the least correlated. Dark shade indicates the secondary features, obtained from the primary features reported in Table 1 with simple algebra.

Table 1. Primary features used in the statistical analysis. VBM indicates the valence band maximum.

Descriptor	Details	Abbreviation
M-O	Bulk average M-O distance (M=transition metal in ternary compounds)	d(M-L)
q(M)	Bulk metal Bader charge (M=transition metal in ternary compounds)	q(M)
q(L)	Bulk ligand Bader charge	q(L)
L(p) band center	Bulk ligand p band (vs E_F for conductors, vs VBM for insulators)	L(p)
$L(p)_{filled}$ band center	Bulk ligand p band center, filled states (vs E_F for conductors, vs VBM for insulators)	L(p)-f
M(d) band center[a]	Bulk metal d band center (M=transition metal in ternary compounds) (vs E_F for conductors, vs VBM for insulators)	M(d)
$M(d)_{filled}$ band center[a]	Bulk metal d band center (M=transition metal in ternary compounds), filled states (vs E_F for conductors, vs VBM for insulators)	M(d)-f
$M(d)_{empty}$ band center[a]	Bulk metal d band center (M=transition metal in ternary compounds), empty states (vs E_F for conductors, vs VBM for insulators)	M(d)-e
Band gap	Bulk DFT-computed band gap	Gap
Ligand Band width	Bulk ligand Band width	BW
Electronegativity difference	Averaged bond ionicity based on Pauling electronegativity	Ion
Surface L(p) band center	Surface ligand p band center (vs E_F for conductors, vs VBM for insulators)	L(p)-surf
Surface metal (d) band center[a]	Surface metal *d* band center (vs E_F for conductors, vs VBM for insulators)	M(d)-surf
Surface band gap	DFT-computed band gap of slab calculation	Gap-surf
Work function	Work function of the clean surface for conductors, position of VBM with respect to vacuum level for insulators	WF
Work function with adsorbed H	Work function of the surface with adsorbed H	WF-H

[a] All states (s, p and d) for non transition metals

We first considered the performance of these physical properties as single descriptors. Figure 6 reports the mean absolute error for the 28 features (see Figure S3 for the performance of additional features). We found the surface ligand band center referenced to the bottom of the conduction band for semiconductors and insulators to be the single variable feature which best correlates with the hydrogen adsorption energy. Bulk and surface ligand band centers referenced to either mid-gap or the bottom of the conduction band work reasonably well as single descriptors. Other significant features are the work function referenced to the CBM, the band gap (bulk and surface), the ligand charge, and

the computed charge transfer gap. Interestingly, other properties such as the band width have lower significance in this analysis. The analysis of the coefficients, *i.e.* of the slopes of the linear fit (Figure S5 and S6) reveals that most of the ligand properties, band centers and charges, work function and band width have negative or negligible coefficients, as shown in Figure 3 for the bulk ligand *p* band center referenced to mid-gap and they are thus inversely correlated with the hydrogen adsorption energy. Conversely, the coefficients of metal band centers are generally small and reference-dependent, whereas the band gap, charge transfer gap and ionicity show a positive correlation (Figure S5). Further confirmation of the feature importance comes from the Random Forest regression analysis (Figure S7) of the 28 features reported in Figure 6, which indicates the ligand *p* band centers L(p)** and L(p)-surf**, the work function WF**, the ligand charge q(L), and the work function with adsorbed hydrogen WF-H as the most relevant features.

The similarity between some of the single variable linear regressions (Figure S6) suggests that they are correlated and multiple descriptors should be considered together. We have then considered multi-variable linear regression analysis, without and with different regularizations, namely LASSO, Ridge and Elastic Net with different mixing parameter α = 0.25, 0.50, 0.75 (EN1, EN2, and EN3, respectively). For this analysis, the data were randomly divided in a training set (80% of data) and test set (20% of data), and a 5-fold cross validation was used to train the data for the regularized methods. The performance of the different regression methods on the test set is shown in Figure 7a and Figures S8-13. The results show that the regularized regression methods (in particular Ridge and EN1, Figures S10 and S11) perform best on our dataset. EN2, EN3 and LASSO (Figures S9, S12 and S13) performs slightly worse, with a MAE comparable to Random Forest (Figure S7) and lower than unregularized linear regression (Figure S8), though LASSO gives a sparser solution compared to Ridge. The somewhat worse performance of Random Forest compared to regularized methods on our data is most likely due the difficulty of tree-based techniques in general to capture a linear relationship between input features and target variable.[102] We note that the inclusion of three features (L(p)-surf, Gap-surf and d(M-L)), performs relatively well, indicating that these are the most relevant features needed to capture the hydrogen adsorption energetics. This is further confirmed by the feature importance for the multi-variable linear regressions (Figure 7b) evaluated as the absolute value of the coefficients, which indicates these three descriptors as the most relevant. Among the descriptors that have minor relevance and can be disregarded, we identify the metal Bader charge and the bond ionicity.

The statistical analysis provides useful insights on the physical properties underlying the affinity for hydrogen. The surface ligand *p* band and band gap, already identified in the single-variable linear regression as relevant when combined (L(p)-surf** feature), are confirmed by the regularized regression models to have coefficients with opposite sign, validating our intuition that the DOS should be corrected by the band gap when studying the adsorption of an electron donor. Conversely, the bulk average M-L distance was less relevant as single feature descriptors, while appears to be important in combination with the other features. We note that the M-L distance strongly influence the electrostatic potential of the ionic material, which can explain why it is required for an accurate prediction of the hydrogen binding energy, as it can account for the difference between material families. Interestingly, other properties which could potentially relevant for the hydrogen adsorption energy, such as the work function of the bare surface and the surface with adsorbed hydrogen, have a lower predictive power compared to the position of the ligand states. We attribute this failure to the difficulty of these descriptors to deal with the presence of a band gap. In particular, the work function of the bare surface is a good measure of the electron acceptor level for metals, while in case of band gap material it is computed as the position of the top of the valence band with respect to the vacuum level, which is not relevant for the oxidative adsorption studied here. The work function referenced to the CBM and the work function of the surface with adsorbed hydrogen are better descriptors for the electron acceptor level and indeed perform well as single features, but they do not show up in the multivariable analysis. We note that although the band gap is not well reproduced at PBE level, its occurrence in the description of the H adsorption energy has a clear physical meaning, as it accounts for the different acceptor levels in insulating and semiconducting materials compared to metals, which does not depend on the exact value of the band gap. In perspective, more work has to be done to develop theoretical methods able to quantitatively describe these features without relying on material-depend parameters.

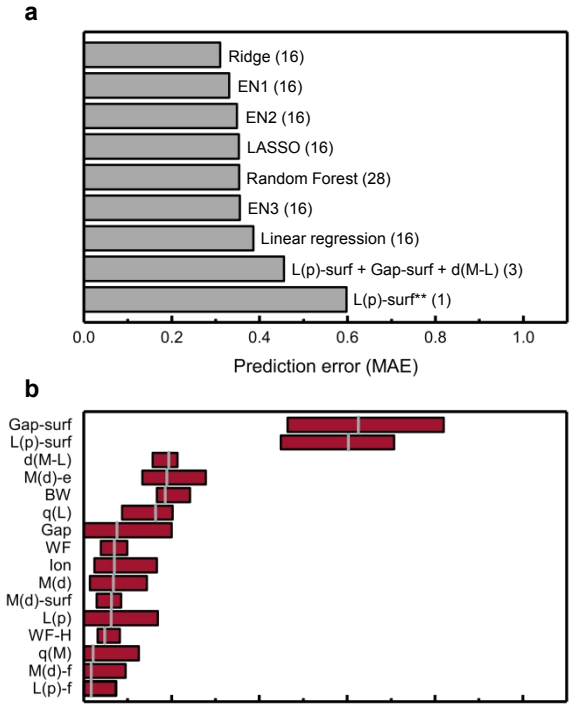

Figure 7. Comparison of the predictive ability and relative importance of descriptors for different QSPR. (a) Prediction error for the different QSPRs considered in this work, which include single and multiple variable linear regression, Random Forest regression and regularized linear regression methods LASSO, Ridge and Elastic Net with mixing parameter α = 0.25, 0.50, 0.75 (EN1, EN2, and EN3, respectively), where 80% of the data were randomly chosen as training set, and 20% as test set. The number of variables included in each QSPR is indicated in bracket. The error is reported as mean absolute error (MAE) on the test set. We note that for the linear regression with the L(p)-surf** variable the MAE is larger compared to the one reported in Figure 6, which

represent the training error on the whole dataset. (b) Relative importance of the descriptors included in the multivariable linear regression, Lasso, Ridge and Elastic Net regression with mixing parameters α = 0.25, 0.50, 0.75. The relative importance is estimated as $|\beta|$, where β are the coefficients of the linear model for each method. The 16 primary features included in the analysis are: average bulk metal-ligand distance (d(M-L)), bulk metal and ligand Bader charges (q(M) and q(L)), the ligand *p* band center (L(p)) and band width (BW), the filled states ligand *p* band center (L(p)-f), the metal *d* band center (M(d)), bulk filled and empty states metal d band center (M(d)-f and M(d)-e), bulk DFT band gap (Gap), ionicity (Ion), surface ligand *p* band center (L(p)-surf), surface metal *d* band center (M(d)-surf), surface band gap (Gap-surf), surface work function (WF) and the work function of the surface with adsorbed hydrogen (WF-H). Range and mean of the values obtained with the different regression models are represented by the bars and the gray lines, respectively.

The results reported above have several implications. First, the charge state of adsorbed hydrogen atoms on inorganic materials is strongly dependent on the electronic structure. Hydrogen adsorbs as H^0 on materials with large band gap, where the hydrogen level falls below the conduction band minimum. As the hydrogen level is positioned at -4.5 eV on the absolute energy scale,[103,104] it has been predicted that in the bulk of crystalline oxides with band gap larger than 5.5 eV the hydrogen neutral form can exist as an interstitial defect.[103] In agreement with this view, we found hydrogen to be adsorbed in its neutral form on materials with high band gap. In all other cases, hydrogen adsorbs as H^+ on the anionic ligand and an electron into the conduction band or at localized states close to the conduction band. This general trend can be complicated by the presence of defects, which can introduce additional trapping levels in the band gap,[105,106] disorder, as reported for the hydrogen defect on amorphous silica,[107,108] or coadsorbed species which allows for Lewis acid/base pair adsorption.[109] Secondly, the descriptors that we have identified for the hydrogen adsorption energy, which rely on the position of the ligand states, the band gap and the metal-ligand bond length, can serve to identify and predict materials with adsorption properties suitable for a given applications. For instance, materials with high hydrogen binding energy are expected to have a low C-H breaking activation barrier (Figure 1e) for the oxidative C-H activation of hydrocarbon. Late transition metal oxides (i.e. Ni-containing oxides), and oxides with transition metals in high oxidation state, would fulfill this requirement. On the other hand, insulating oxides, phosphates and fluorides have a low affinity for hydrogen and would be the materials of choice in the design of inert electrodes or coatings to prevent interfacial chemical oxidation of organic solvents. Among these materials, we find material already reported as effective coatings for positive electrodes in Li-ion batteries, such as Al_2O_3, TiO_2, ZrO_2, HfO_2,[110,111] and fluorides, such as NiF_2, MnF_2 and CoF_2 which could form from the decomposition of F-containing electrolyte salts (i. e. $LiPF_6$) at the surface of electrodes containing these transition metals.

CONCLUSIONS

The hydrogen adsorption energy and ligand vacancy formation energies on the surfaces of ionic compounds used for materials for energy conversion and storage have been computed by DFT. Our results show that the hydrogen adsorption energy correlates with the ligand *p* band center, where materials with ligand *p* band center higher in energy, *i.e.* closer to the Fermi level, have an increased affinity for hydrogen adsorption. This correlation is dictated by the electron transfer occurring upon H adsorption for all materials except high band gap insulators, where electrons are effectively transferred from the ligand states to the metal states, and explain why the adsorption is more favorable on reducible or metallic oxides. The ligand vacancy formation energy follows the same trend, and strongly correlated with the hydrogen adsorption energy, where both of the properties depend on the substrate reduction tendency. A statistical regression analysis allows us to further demonstrate that a combination of descriptors, including structural and electronic properties, are necessary to predict the hydrogen adsorption energy of ionic materials. The most relevant descriptors were identified to be the ligand *p* band center, the band gap and metal-ligand distance. These material properties can be used to predict the hydrogen affinity in future high-throughput studies with the goal of identifying new positive electrodes or coatings materials for Li-ion batteries as well as high-performant catalysts for H-H and C-H activation.

ASSOCIATED CONTENT

Supporting Information

The Supporting Information is available free of charge on the ACS Publications website.

List of space groups and surface orientation of computed compounds, schematic representation of band structure, density of states of selected compounds, additional details on the statistical analysis (PDF).

AUTHOR INFORMATION

Corresponding Author

* (L. G.) Email: lgiordan@mit.edu
* (Y. S.-H.) Email: shaohorn@mit.edu

ACKNOWLEDGMENT

The research was supported by BMW Technology Corporation. This research used resources of the National Energy Research Scientific Computing Center, a DOE Office of Science User Facility supported by the Office of Science of the U.S. Department of Energy under Contract No. DE-AC02-05CH11231. This work also used resources of the Extreme Science and Engineering Discovery Environment (XSEDE),[112] which is supported by National Science Foundation grant number ACI-1548562.

REFERENCES

1. Mizushima, K.; Jones, P. C.; Wiseman, P. J.; Goodenough, J. B. LixCoO2 (0<x~l): A New Cathode Material for Batteries of High Energy Density. *Mater. Res. Bull.* **1980**, *15* (6), 783–789.
2. Suntivich, J.; May, K. J.; Gasteiger, H. A.; Goodenough, J. B.; Shao-Horn, Y. A Perovskite Oxide Optimized for Oxygen Evolution Catalysis from Molecular Orbital Principles. *Science* **2011**, *334* (6061), 1383–1385. https://doi.org/10.1126/science.1211927.
3. Huang, H.; Yin, S.-C.; Nazar, L. F. Approaching Theoretical Capacity of $LiFePO_4$ at Room Temperature at High Rates. *Electrochem. Solid-State Lett.* **2001**, *4* (10), A170. https://doi.org/10.1149/1.1396695.
4. Kang, B.; Ceder, G. Battery Materials for Ultrafast

Charging and Discharging. *Nature* **2009**, *458* (7235), 190–193. https://doi.org/10.1038/nature07853.

5. Badway, F.; Cosandey, F.; Pereira, N.; Amatucci, G. G. Carbon Metal Fluoride Nanocomposites. *J. Electrochem. Soc.* **2003**, *150* (10), A1318. https://doi.org/10.1149/1.1602454.
6. Whittingham, M. S. Electrical Energy Storage and Intercalation Chemistry. *Science* **1976**, *192*, 1126–1127.
7. Sakuda, A.; Takeuchi, T.; Okamura, K.; Kobayashi, H.; Sakaebe, H.; Tatsumi, K.; Ogumi, Z. Rock-Salt-Type Lithium Metal Sulphides as Novel Positive-Electrode Materials. *Sci. Rep.* **2015**, *4* (1). https://doi.org/10.1038/srep04883.
8. Goodenough, J. B.; Park, K.-S. The Li-Ion Rechargeable Battery: A Perspective. *J. Am. Chem. Soc.* **2013**, *135* (4), 1167–1176. https://doi.org/10.1021/ja3091438.
9. Tarascon, J.-M.; Armand, M. Issues and Challenges Facing Rechargeable Lithium Batteries. *Nature* **2001**, *414* (6861), 359–367.
10. Armand, M.; Tarascon, J.-M. Building Better Batteries. *Nature* **2008**, *451* (7179), 652–657.
11. Winter, M.; Barnett, B.; Xu, K. Before Li Ion Batteries. *Chem. Rev.* **2018**, *118* (23), 11433–11456. https://doi.org/10.1021/acs.chemrev.8b00422.
12. Lewis, N. S.; Nocera, D. G. Powering the Planet: Chemical Challenges in Solar Energy Utilization. *Proc. Natl. Acad. Sci. U. S. Am. PNAS Proc. Natl. Acad. Sci.* **2006**, *103* (43), 15729–15735.
13. Greeley, J.; Markovic, N. M. The Road from Animal Electricity to Green Energy: Combining Experiment and Theory in Electrocatalysis. *Energy Environ. Sci.* **2012**, *5* (11), 9246. https://doi.org/10.1039/c2ee21754f.
14. Hong, W. T.; Risch, M.; Stoerzinger, K. A.; Grimaud, A.; Suntivich, J.; Shao-Horn, Y. Toward the Rational Design of Non-Precious Transition Metal Oxides for Oxygen Electrocatalysis. *Energy Env. Sci* **2015**, *8* (5), 1404–1427. https://doi.org/10.1039/C4EE03869J.
15. Horn, R.; Schlögl, R. Methane Activation by Heterogeneous Catalysis. *Catal. Lett.* **2015**, *145* (1), 23–39. https://doi.org/10.1007/s10562-014-1417-z.
16. Carrero, C. A.; Schloegl, R.; Wachs, I. E.; Schomaecker, R. Critical Literature Review of the Kinetics for the Oxidative Dehydrogenation of Propane over Well-Defined Supported Vanadium Oxide Catalysts. *ACS Catal.* **2014**, *4* (10), 3357–3380. https://doi.org/10.1021/cs5003417.
17. Liang, Z.; Li, T.; Kim, M.; Asthagiri, A.; Weaver, J. F. Low-Temperature Activation of Methane on the IrO_2 (110) Surface. *Science* **2017**, *356* (6335), 299–303. https://doi.org/10.1126/science.aam9147.
18. Goodenough, J. B. Oxide Cathodes. In *Advances in lithium-ion batteries*; Kluwer Academic/Plenum Publishers: New York, 2002; Vol. Cap. 4.
19. Goodenough, J. B.; Kim, Y. Challenges for Rechargeable Li Batteries. *Chem. Mater.* **2010**, *22* (3), 587–603. https://doi.org/10.1021/cm901452z.
20. Wolverton, C.; Zunger, A. Prediction of Li Intercalation and Battery Voltages in Layered vs. Cubic Li x CoO2. *J. Electrochem. Soc.* **1998**, *145* (7), 2424–2431.
21. Padlhi, A. K.; Nanjundaswamy, K. S.; Masquelier, C.; Okada, S.; Goodenough, J. B. Effect of Structure on the Fe3/Fe2 Recdlox Couple in Iron Phosphates. *J Electrochem Soc* **1997**, *144* (5), 5.
22. Zhou, F.; Cococcioni, M.; Kang, K.; Ceder, G. The Li Intercalation Potential of LiMPO4 and LiMSiO4 Olivines with M=Fe, Mn, Co, Ni. *Electrochem. Commun.* **2004**, *6* (11), 1144–1148. https://doi.org/10.1016/j.elecom.2004.09.007.
23. Doublet, M.-L.; Lemoigno, F.; Gillot, F.; Monconduit, L. The $Li_x VPn_4$ Ternary Phases (Pn = P, As): Rigid Networks for Lithium Intercalation/Deintercalation. *Chem. Mater.* **2002**, *14* (10), 4126–4133. https://doi.org/10.1021/cm020047e.
24. Calle-Vallejo, F.; Loffreda, D.; Koper, M. T. M.; Sautet, P. Introducing Structural Sensitivity into Adsorption–Energy Scaling Relations by Means of Coordination Numbers. *Nat. Chem.* **2015**, *7* (5), 403–410. https://doi.org/10.1038/nchem.2226.
25. Abild-Pedersen, F.; Greeley, J.; Studt, F.; Rossmeisl, J.; Munter, T. R.; Moses, P. G.; Skúlason, E.; Bligaard, T.; Nørskov, J. K. Scaling Properties of Adsorption Energies for Hydrogen-Containing Molecules on Transition-Metal Surfaces. *Phys. Rev. Lett.* **2007**, *99* (1). https://doi.org/10.1103/PhysRevLett.99.016105.
26. Rossmeisl, J.; Qu, Z.-W.; Zhu, H.; Kroes, G.-J.; Nørskov, J. K. Electrolysis of Water on Oxide Surfaces. *J. Electroanal. Chem.* **2007**, *607* (1–2), 83–89. https://doi.org/10.1016/j.jelechem.2006.11.008.
27. Man, I. C.; Su, H.-Y.; Calle-Vallejo, F.; Hansen, H. A.; Martínez, J. I.; Inoglu, N. G.; Kitchin, J.; Jaramillo, T. F.; Nørskov, J. K.; Rossmeisl, J. Universality in Oxygen Evolution Electrocatalysis on Oxide Surfaces. *ChemCatChem* **2011**, *3* (7), 1159–1165. https://doi.org/10.1002/cctc.201000397.
28. Nørskov, J. K.; Bligaard, T.; Rossmeisl, J.; Christensen, C. H. Towards the Computational Design of Solid Catalysts. *Nat. Chem.* **2009**, *1* (1), 37–46. https://doi.org/10.1038/nchem.121.
29. Grimaud, A.; Hong, W. T.; Shao-Horn, Y.; Tarascon, J.-M. Anionic Redox Processes for Electrochemical Devices. *Nat. Mater.* **2016**, *15* (2), 121–126.
30. Sathiya, M.; Rousse, G.; Ramesha, K.; Laisa, C. P.; Vezin, H.; Sougrati, M. T.; Doublet, M.-L.; Foix, D.; Gonbeau, D.; Walker, W.; et al. Reversible Anionic Redox Chemistry in High-Capacity Layered-Oxide Electrodes. *Nat. Mater.* **2013**, *12* (9), 827–835. https://doi.org/10.1038/nmat3699.
31. McCalla, E.; Abakumov, A. M.; Saubanère, M.; Foix, D.; Berg, E. J.; Rousse, G.; Doublet, M.-L.; Gonbeau, D.; Novák, P.; Van Tendeloo, G.; et al. Visualization of O-O Peroxo-like Dimers in High-Capacity Layered Oxides for Li-Ion Batteries. *Science* **2015**, *350* (6267), 1516–1521. https://doi.org/10.1126/science.aad1080.
32. Rouxel, J. Anion–Cation Redox Competition and the Formation of New Compounds in Highly Covalent Systems. *Chem. - Eur. J.* **1996**, *2* (9), 1053–1059. https://doi.org/10.1002/chem.19960020904.
33. Berry, J. F. Two-Center/Three-Electron Sigma Half-Bonds in Main Group and Transition Metal Chemistry. *Acc. Chem. Res.* **2016**, *49* (1), 27–34. https://doi.org/10.1021/acs.accounts.5b00517.
34. Jung, R.; Metzger, M.; Maglia, F.; Stinner, C.; Gasteiger, H. A. Oxygen Release and Its Effect on the Cycling Stability of LiNixMnyCozO2 (NMC) Cathode Materials for Li-Ion Batteries. *J. Electrochem. Soc.* **2017**, *164* (7), A1361–A1377.
35. Jung, R.; Metzger, M.; Maglia, F.; Stinner, C.; Gasteiger, H. A. Chemical versus Electrochemical Electrolyte Oxidation on NMC111, NMC622, NMC811, LNMO, and Conductive Carbon. *J. Phys. Chem. Lett.* **2017**, *8* (19), 4820–4825. https://doi.org/10.1021/acs.jpclett.7b01927.
36. Kim, U.-H.; Jun, D.-W.; Park, K.-J.; Zhang, Q.; Kaghazchi, P.; Aurbach, D.; Major, D. T.; Goobes, G.; Dixit, M.; Leifer, N.; et al. Pushing the Limit of Layered Transition Metal Oxide Cathodes for High-Energy Density Rechargeable Li Ion Batteries. *Energy Environ. Sci.* **2018**, *11* (5), 1271–1279. https://doi.org/10.1039/C8EE00227D.
37. Vetter, J.; Novák, P.; Wagner, M. R.; Veit, C.; Möller, K.-C.; Besenhard, J. O.; Winter, M.; Wohlfahrt-Mehrens, M.; Vogler, C.; Hammouche, A. Ageing Mechanisms in Lithium-Ion Batteries. *J. Power Sources* **2005**, *147* (1–2), 269–281. https://doi.org/10.1016/j.jpowsour.2005.01.006.

38. Xu, K. Nonaqueous Liquid Electrolytes for Lithium-Based Rechargeable Batteries. *Chem. Rev.* **2004**, *104* (10), 4303–4418. https://doi.org/10.1021/cr030203g.
39. Xu, K. Electrolytes and Interphases in Li-Ion Batteries and Beyond. *Chem. Rev.* **2014**, *114* (23), 11503–11618. https://doi.org/10.1021/cr500003w.
40. Gauthier, M.; Carney, T. J.; Grimaud, A.; Giordano, L.; Pour, N.; Chang, H.-H.; Fenning, D. P.; Lux, S. F.; Paschos, O.; Bauer, C.; et al. Electrode–Electrolyte Interface in Li-Ion Batteries: Current Understanding and New Insights. *J. Phys. Chem. Lett.* **2015**, *6* (22), 4653–4672. https://doi.org/10.1021/acs.jpclett.5b01727.
41. Giordano, L.; Karayaylali, P.; Yu, Y.; Katayama, Y.; Maglia, F.; Lux, S.; Shao-Horn, Y. Chemical Reactivity Descriptor for the Oxide-Electrolyte Interface in Li-Ion Batteries. *J. Phys. Chem. Lett.* **2017**, *8* (16), 3881–3887. https://doi.org/10.1021/acs.jpclett.7b01655.
42. Sathiya, M.; Ramesha, K.; Rousse, G.; Foix, D.; Gonbeau, D.; Prakash, A. S.; Doublet, M. L.; Hemalatha, K.; Tarascon, J.-M. High Performance $Li_2Ru_{1-y}Mn_yO_3$ ($0.2 \leq y \leq 0.8$) Cathode Materials for Rechargeable Lithium-Ion Batteries: Their Understanding. *Chem. Mater.* **2013**, *25* (7), 1121–1131. https://doi.org/10.1021/cm400193m.
43. Seo, D.-H.; Lee, J.; Urban, A.; Malik, R.; Kang, S.; Ceder, G. The Structural and Chemical Origin of the Oxygen Redox Activity in Layered and Cation-Disordered Li-Excess Cathode Materials. *Nat. Chem.* **2016**, *8* (7), 692–697. https://doi.org/10.1038/nchem.2524.
44. Luo, K.; Roberts, M. R.; Hao, R.; Guerrini, N.; Pickup, D. M.; Liu, Y.-S.; Edström, K.; Guo, J.; Chadwick, A. V.; Duda, L. C.; et al. Charge-Compensation in 3d-Transition-Metal-Oxide Intercalation Cathodes through the Generation of Localized Electron Holes on Oxygen. *Nat. Chem.* **2016**, *8* (7), 684–691. https://doi.org/10.1038/nchem.2471.
45. Gent, W. E.; Lim, K.; Liang, Y.; Li, Q.; Barnes, T.; Ahn, S.-J.; Stone, K. H.; McIntire, M.; Hong, J.; Song, J. H.; et al. Coupling between Oxygen Redox and Cation Migration Explains Unusual Electrochemistry in Lithium-Rich Layered Oxides. *Nat. Commun.* **2017**, *8* (1). https://doi.org/10.1038/s41467-017-02041-x.
46. Grimaud, A.; Diaz-Morales, O.; Han, B.; Hong, W. T.; Lee, Y.-L.; Giordano, L.; Stoerzinger, K. A.; Koper, M. T. M.; Shao-Horn, Y. Activating Lattice Oxygen Redox Reactions in Metal Oxides to Catalyse Oxygen Evolution. *Nat. Chem.* **2017**, *9* (5), 457–465. https://doi.org/10.1038/nchem.2695.
47. Fung, V.; Polo-Garzon, F.; Wu, Z.; Jiang, D. Exploring Perovskites for Methane Activation from First Principles. *Catal. Sci. Technol.* **2018**, *8* (3), 702–709. https://doi.org/10.1039/C7CY01791J.
48. Kumar, G.; Lau, S. L. J.; Krcha, M. D.; Janik, M. J. Correlation of Methane Activation and Oxide Catalyst Reducibility and Its Implications for Oxidative Coupling. *ACS Catal.* **2016**, *6* (3), 1812–1821. https://doi.org/10.1021/acscatal.5b02657.
49. Rivadulla, F.; Zhou, J.-S.; Goodenough, J. B. Chemical, Structural, and Transport Properties of Na 1 − x CoO 2. *Phys. Rev. B* **2003**, *68* (7). https://doi.org/10.1103/PhysRevB.68.075108.
50. Zaanen, J.; Sawatzky, G. A.; Allen, J. W. Band Gaps and Electronic Structure of Transition-Metal Compounds. *Phys. Rev. Lett.* **1985**, *55* (4), 418–421. https://doi.org/10.1103/PhysRevLett.55.418.
51. Rouxel, J.; Toumoux, M. Chimie Deuce with Solid Precursors, Past and Present. *Solid State Ion.* **1996**, *84*, 141–149.
52. Rouxel, J.; Brec, R. Low-Dimensional Chalcogenides as Secondary Cathodic Materials: Some Geometric and Electronic Aspects. *Annu. Rev. Mater. Sci.* **1986**, *16* (1), 137–162.
53. Goodenough, J. B. Oxygen Ordering, Peroxide Ion Formation, and Polarization Fluctuations in YBa2Cu3O7-d. *Mater. Res. Bull.* **1988**, *23*, 401–412.
54. Hong, W. T.; Stoerzinger, K. A.; Moritz, B.; Devereaux, T. P.; Yang, W.; Shao-Horn, Y. Probing $LaMO_3$ Metal and Oxygen Partial Density of States Using X-Ray Emission, Absorption, and Photoelectron Spectroscopy. *J. Phys. Chem. C* **2015**, *119* (4), 2063–2072. https://doi.org/10.1021/jp511931y.
55. Abraham, D. P.; Twesten, R. D.; Balasubramanian, M.; Kropf, J.; Fischer, D.; McBreen, J.; Petrov, I.; Amine, K. Microscopy and Spectroscopy of Lithium Nickel Oxide-Based Particles Used in High Power Lithium-Ion Cells. *J. Electrochem. Soc.* **2003**, *150* (11), A1450. https://doi.org/10.1149/1.1613291.
56. Liu, H.; Bugnet, M.; Tessaro, M. Z.; Harris, K. J.; Dunham, M. J. R.; Jiang, M.; Goward, G. R.; Botton, G. A. Spatially Resolved Surface Valence Gradient and Structural Transformation of Lithium Transition Metal Oxides in Lithium-Ion Batteries. *Phys Chem Chem Phys* **2016**, *18* (42), 29064–29075. https://doi.org/10.1039/C6CP05262B.
57. Lin, F.; Markus, I. M.; Nordlund, D.; Weng, T.-C.; Asta, M. D.; Xin, H. L.; Doeff, M. M. Surface Reconstruction and Chemical Evolution of Stoichiometric Layered Cathode Materials for Lithium-Ion Batteries. *Nat. Commun.* **2014**, *5*. https://doi.org/10.1038/ncomms4529.
58. Hwang, S.; Chang, W.; Kim, S. M.; Su, D.; Kim, D. H.; Lee, J. Y.; Chung, K. Y.; Stach, E. A. Investigation of Changes in the Surface Structure of $Li_xNi_{0.8}Co_{0.15}Al_{0.05}O_2$ Cathode Materials Induced by the Initial Charge. *Chem. Mater.* **2014**, *26* (2), 1084–1092. https://doi.org/10.1021/cm403332s.
59. Wandt, J.; Freiberg, A. T. S.; Ogrodnik, A.; Gasteiger, H. A. Singlet Oxygen Evolution from Layered Transition Metal Oxide Cathode Materials and Its Implications for Lithium-Ion Batteries. *Mater. Today* **2018**. https://doi.org/10.1016/j.mattod.2018.03.037.
60. Mahne, N.; Schafzahl, B.; Leypold, C.; Leypold, M.; Grumm, S.; Leitgeb, A.; Strohmeier, G. A.; Wilkening, M.; Fontaine, O.; Kramer, D.; et al. Singlet Oxygen Generation as a Major Cause for Parasitic Reactions during Cycling of Aprotic Lithium–Oxygen Batteries. *Nat. Energy* **2017**, *2* (5). https://doi.org/10.1038/nenergy.2017.36.
61. Pearce, P. E.; Perez, A. J.; Rousse, G.; Saubanère, M.; Batuk, D.; Foix, D.; McCalla, E.; Abakumov, A. M.; Van Tendeloo, G.; Doublet, M.-L.; et al. Evidence for Anionic Redox Activity in a Tridimensional-Ordered Li-Rich Positive Electrode β-Li2IrO3. *Nat. Mater.* **2017**, *16* (5), 580–586. https://doi.org/10.1038/nmat4864.
62. Yabuuchi, N.; Nakayama, M.; Takeuchi, M.; Komaba, S.; Hashimoto, Y.; Mukai, T.; Shiiba, H.; Sato, K.; Kobayashi, Y.; Nakao, A.; et al. Origin of Stabilization and Destabilization in Solid-State Redox Reaction of Oxide Ions for Lithium-Ion Batteries. *Nat. Commun.* **2016**, *7* (1). https://doi.org/10.1038/ncomms13814.
63. Lee, J.; Kitchaev, D. A.; Kwon, D.-H.; Lee, C.-W.; Papp, J. K.; Liu, Y.-S.; Lun, Z.; Clément, R. J.; Shi, T.; McCloskey, B. D.; et al. Reversible Mn2+/Mn4+ Double Redox in Lithium-Excess Cathode Materials. *Nature* **2018**, *556* (7700), 185–190. https://doi.org/10.1038/s41586-018-0015-4.
64. House, R. A.; Jin, L.; Maitra, U.; Tsuruta, K.; Somerville, J. W.; Förstermann, D. P.; Massel, F.; Duda, L.; Roberts, M. R.; Bruce, P. G. Lithium Manganese Oxyfluoride as a New Cathode Material Exhibiting Oxygen Redox. *Energy Environ. Sci.* **2018**, *11* (4), 926–932. https://doi.org/10.1039/C7EE03195E.

65. Mefford, J. T.; Rong, X.; Abakumov, A. M.; Hardin, W. G.; Dai, S.; Kolpak, A. M.; Johnston, K. P.; Stevenson, K. J. Water Electrolysis on La1−xSr x CoO3−δ Perovskite Electrocatalysts. *Nat. Commun.* **2016**, *7* (1). https://doi.org/10.1038/ncomms11053.
66. Matsumoto, Y.; Sato, E. Electrocatalytic Properties of Transition Metal Oxides for Oxygen Evolution Reaction. *Mater. Chem. Phys.* **1986**, *14* (5), 397–426. https://doi.org/10.1016/0254-0584(86)90045-3.
67. Yu, Y.; Karayaylali, P.; Katayama, Y.; Giordano, L.; Gauthier, M.; Maglia, F.; Jung, R.; Lund, I.; Shao-Horn, Y. Coupled LiPF $_6$ Decomposition and Carbonate Dehydrogenation Enhanced by Highly Covalent Metal Oxides in High-Energy Li-Ion Batteries. *J. Phys. Chem. C* **2018**, *122* (48), 27368–27382. https://doi.org/10.1021/acs.jpcc.8b07848.
68. Østergaard, T. M.; Giordano, L.; Castelli, I. E.; Maglia, F.; Antonopoulos, B. K.; Shao-Horn, Y.; Rossmeisl, J. Oxidation of Ethylene Carbonate on Li Metal Oxide Surfaces. *J. Phys. Chem. C* **2018**, *122* (19), 10442–10449. https://doi.org/10.1021/acs.jpcc.8b01713.
69. Kumar, N.; Leung, K.; Siegel, D. J. Crystal Surface and State of Charge Dependencies of Electrolyte Decomposition on LiMn2O4 Cathode. *J. Electrochem. Soc.* **2014**, *161* (8), E3059–E3065.
70. Borodin, O.; Olguin, M.; Spear, C. E.; Leiter, K. W.; Knap, J. Towards High Throughput Screening of Electrochemical Stability of Battery Electrolytes. *Nanotechnology* **2015**, *26* (35), 354003. https://doi.org/10.1088/0957-4484/26/35/354003.
71. Leung, K. First-Principles Modeling of the Initial Stages of Organic Solvent Decomposition on LixMn2O4(100) Surfaces. *J. Phys. Chem. C* **2012**, *116* (18), 9852–9861. https://doi.org/10.1021/jp212415x.
72. Xu, S.; Luo, G.; Jacobs, R.; Fang, S.; Mahanthappa, M. K.; Hamers, R. J.; Morgan, D. Ab Initio Modeling of Electrolyte Molecule Ethylene Carbonate Decomposition Reaction on Li(Ni,Mn,Co)O $_2$ Cathode Surface. *ACS Appl. Mater. Interfaces* **2017**, *9* (24), 20545–20553. https://doi.org/10.1021/acsami.7b03435.
73. Aurbach, D.; Gamolsky, K.; Markovsky, B.; Salitra, G.; Gofer, Y.; Heider, U.; Oesten, R.; Schmidt, M. The Study of Surface Phenomena Related to Electrochemical Lithium Intercalation into Li x MO y Host Materials (M= Ni, Mn). *J. Electrochem. Soc.* **2000**, *147* (4), 1322–1331.
74. Tebbe, J. L.; Fuerst, T. F.; Musgrave, C. B. Degradation of Ethylene Carbonate Electrolytes of Lithium Ion Batteries via Ring Opening Activated by LiCoO $_2$ Cathode Surfaces and Electrolyte Species. *ACS Appl. Mater. Interfaces* **2016**, *8* (40), 26664–26674. https://doi.org/10.1021/acsami.6b06157.
75. Li, B.; Metiu, H. Dissociation of Methane on La $_2$ O $_3$ Surfaces Doped with Cu, Mg, or Zn. *J. Phys. Chem. C* **2011**, *115* (37), 18239–18246. https://doi.org/10.1021/jp2049603.
76. Tian, D.; Li, K.; Wei, Y.; Zhu, X.; Zeng, C.; Cheng, X.; Zheng, Y.; Wang, H. DFT Insights into Oxygen Vacancy Formation and CH $_4$ Activation over CeO $_2$ Surfaces Modified by Transition Metals (Fe, Co and Ni). *Phys. Chem. Chem. Phys.* **2018**, *20* (17), 11912–11929. https://doi.org/10.1039/C7CP08376A.
77. Krcha, M. D.; Mayernick, A. D.; Janik, M. J. Periodic Trends of Oxygen Vacancy Formation and C–H Bond Activation over Transition Metal-Doped CeO2 (111) Surfaces. *J. Catal.* **2012**, *293*, 103–115. https://doi.org/10.1016/j.jcat.2012.06.010.
78. Castelli, I. E.; Man, I.-C.; Soriga, S.-G.; Parvulescu, V.; Halck, N. B.; Rossmeisl, J. Role of the Band Gap for the Interaction Energy of Coadsorbed Fragments. *J. Phys. Chem. C* **2017**, *121* (34), 18608–18614. https://doi.org/10.1021/acs.jpcc.7b04974.
79. Aljama, H.; Nørskov, J. K.; Abild-Pedersen, F. Theoretical Insights into Methane C–H Bond Activation on Alkaline Metal Oxides. *J. Phys. Chem. C* **2017**, *121* (30), 16440–16446. https://doi.org/10.1021/acs.jpcc.7b05838.
80. Latimer, A. A.; Kulkarni, A. R.; Aljama, H.; Montoya, J. H.; Yoo, J. S.; Tsai, C.; Abild-Pedersen, F.; Studt, F.; Nørskov, J. K. Understanding Trends in C–H Bond Activation in Heterogeneous Catalysis. *Nat. Mater.* **2017**, *16* (2), 225–229. https://doi.org/10.1038/nmat4760.
81. Perdew, J. P.; Burke, K.; Ernzerhof, M. Generalized Gradient Approximation Made Simple. *Phys. Rev. Lett.* **1996**, *77* (18), 3865.
82. Kresse, G.; Hafner, J. Ab. Initio Molecular Dynamics for Liquid Metals. *Phys. Rev. B* **1993**, *47*, 558–561.
83. Kresse, G.; Furthmüller, J. Efficient Iterative Schemes for Ab Initio Total-Energy Calculations Using a Plane-Wave Basis Set. *Phys. Rev. B* **1996**, *54* (16), 11169.
84. Anisimov, V. I.; Aryasetiawan, F.; Lichtenstein, A. I. First-Principles Calculations of the Electronic Structure and Spectra of Strongly Correlated Systems: The LDA + U Method. *J. Phys. Condens. Matter* **1997**, *9*, 767–808.
85. Dudarev, S. L.; Botton, G. A.; Savrasov, S. Y.; Humphreys, C. J.; Sutton, A. P. Electron-Energy-Loss Spectra and the Structural Stability of Nickel Oxide: An LSDA+ U Study. *Phys. Rev. B* **1998**, *57* (3), 1505.
86. Becke, A. D. A New Mixing of Hartree–Fock and Local Density-functional Theories. *J. Chem. Phys.* **1993**, *98* (2), 1372–1377. https://doi.org/10.1063/1.464304.
87. Perdew, J. P.; Ernzerhof, M.; Burke, K. Rationale for Mixing Exact Exchange with Density Functional Approximations. *J. Chem. Phys.* **1996**, *105* (22), 9982–9985. https://doi.org/10.1063/1.472933.
88. Wang, L.; Maxisch, T.; Ceder, G. Oxidation Energies of Transition Metal Oxides within the GGA + U Framework. *Phys. Rev. B* **2006**, *73* (19). https://doi.org/10.1103/PhysRevB.73.195107.
89. Lee, Y.-L.; Kleis, J.; Rossmeisl, J.; Morgan, D. *Ab Initio* Energetics of La B O 3 (001) (B = Mn , Fe, Co, and Ni) for Solid Oxide Fuel Cell Cathodes. *Phys. Rev. B* **2009**, *80* (22). https://doi.org/10.1103/PhysRevB.80.224101.
90. He, J.; Franchini, C. Screened Hybrid Functional Applied to 3 d 0 → 3 d 8 Transition-Metal Perovskites La M O 3 (M = Sc–Cu): Influence of the Exchange Mixing Parameter on the Structural, Electronic, and Magnetic Properties. *Phys. Rev. B* **2012**, *86* (23). https://doi.org/10.1103/PhysRevB.86.235117.
91. Bader, R. F. A Quantum Theory of Molecular Structure and Its Applications. *Chem. Rev.* **1991**, *91* (5), 893–928.
92. Tang, W.; Sanville, E.; Henkelman, G. A Grid-Based Bader Analysis Algorithm without Lattice Bias. *J. Phys. Condens. Matter* **2009**, *21* (8), 084204. https://doi.org/10.1088/0953-8984/21/8/084204.
93. Pedregosa, F.; Varoquaux, G.; Gramfort, A.; Michel, V.; Thirion, B.; Grisel, O.; Blondel, M.; Prettenhofer, P.; Weiss, R.; Dubourg, V.; et al. Scikit-Learn: Machine Learning in Python. *Mach. Learn. PYTHON* 6.
94. Di Valentin, C.; Pacchioni, G.; Selloni, A. Electronic Structure of Defect States in Hydroxylated and Reduced Rutile TiO 2 (110) Surfaces. *Phys. Rev. Lett.* **2006**, *97* (16). https://doi.org/10.1103/PhysRevLett.97.166803.
95. Watkins, M. B.; Foster, A. S.; Shluger, A. L. Hydrogen Cycle on CeO $_2$ (111) Surfaces: Density Functional Theory Calculations. *J. Phys. Chem. C* **2007**, *111* (42), 15337–15341. https://doi.org/10.1021/jp071715s.
96. Dedryvère, R.; Martinez, H.; Leroy, S.; Lemordant, D.; Bonhomme, F.; Biensan, P.; Gonbeau, D. Surface Film Formation on Electrodes in a LiCoO2/Graphite Cell: A Step by Step XPS Study. *J. Power Sources* **2007**, *174* (2), 462–468. https://doi.org/10.1016/j.jpowsour.2007.06.033.
97. Gauthier, M.; Karayaylali, P.; Giordano, L.; Feng, S.; Lux, S. F.; Maglia, F.; Lamp, P.; Shao-Horn, Y. Probing Surface

Chemistry Changes Using $LiCoO_2$ -Only Electrodes in Li-Ion Batteries. *J. Electrochem. Soc.* **2018**, *165* (7), A1377–A1387. https://doi.org/10.1149/2.0431807jes.

98. Lee, Y.-L.; Kleis, J.; Rossmeisl, J.; Shao-Horn, Y.; Morgan, D. Prediction of Solid Oxide Fuel Cell Cathode Activity with First-Principles Descriptors. *Energy Environ. Sci.* **2011**, *4* (10), 3966. https://doi.org/10.1039/c1ee02032c.
99. Chrétien, S.; Metiu, H. Acid–Base Interaction and Its Role in Alkane Dissociative Chemisorption on Oxide Surfaces. *J. Phys. Chem. C* **2014**, *118* (47), 27336–27342. https://doi.org/10.1021/jp507207b.
100. Chase, M. W., Jr. NIST-JANAF Themochemical Tables, Fourth Edition. *J Phys Chem Ref Data* **1998**, *Monograph 9*, 1–1951.
101. Fung, V.; Tao, F. F.; Jiang, D. General Structure–Reactivity Relationship for Oxygen on Transition-Metal Oxides. *J. Phys. Chem. Lett.* **2017**, *8* (10), 2206–2211. https://doi.org/10.1021/acs.jpclett.7b00861.
102. Hastie, T.; Tibshirani, R.; Friedman, J. *The Elements of Statistical Learning: Data Mining, Inference and Prediction*; Springer-Verlag, 2009.
103. Van de Walle, C. G. Universal Alignment of Hydrogen Levels in Semiconductors and Insulators. *Phys. B Condens. Matter* **2006**, *376–377*, 1–6. https://doi.org/10.1016/j.physb.2005.12.004.
104. Li, H.; Robertson, J. Behaviour of Hydrogen in Wide Band Gap Oxides. *J. Appl. Phys.* **2014**, *115* (20), 203708. https://doi.org/10.1063/1.4878415.
105. Ricci, D.; Di Valentin, C.; Pacchioni, G.; Sushko, P. V.; Shluger, A. L.; Giamello, E. Paramagnetic Defect Centers at the MgO Surface. An Alternative Model to Oxygen Vacancies. *J. Am. Chem. Soc.* **2003**, *125* (3), 738–747. https://doi.org/10.1021/ja0282240.
106. Kaviani, M.; Afanas'ev, V. V.; Shluger, A. L. Interactions of Hydrogen with Amorphous Hafnium Oxide. *Phys. Rev. B* **2017**, *95* (7). https://doi.org/10.1103/PhysRevB.95.075117.
107. El-Sayed, A.-M.; Watkins, M. B.; Grasser, T.; Afanas'ev, V. V.; Shluger, A. L. Hydrogen-Induced Rupture of Strained Si─O Bonds in Amorphous Silicon Dioxide. *Phys. Rev. Lett.* **2015**, *114* (11). https://doi.org/10.1103/PhysRevLett.114.115503.
108. El-Sayed, A.-M.; Wimmer, Y.; Goes, W.; Grasser, T.; Afanas'ev, V. V.; Shluger, A. L. Theoretical Models of Hydrogen-Induced Defects in Amorphous Silicon Dioxide. *Phys. Rev. B* **2015**, *92* (1). https://doi.org/10.1103/PhysRevB.92.014107.
109. Castelli, I. E.; Man, I.-C.; Soriga, S.-G.; Parvulescu, V.; Halck, N. B.; Rossmeisl, J. Role of the Band Gap for the Interaction Energy of Coadsorbed Fragments. *J. Phys. Chem. C* **2017**, *121* (34), 18608–18614. https://doi.org/10.1021/acs.jpcc.7b04974.
110. Chen, Z.; Qin, Y.; Amine, K.; Sun, Y.-K. Role of Surface Coating on Cathode Materials for Lithium-Ion Batteries. *J. Mater. Chem.* **2010**, *20* (36), 7606. https://doi.org/10.1039/c0jm00154f.
111. Aykol, M.; Kim, S.; Hegde, V. I.; Snydacker, D.; Lu, Z.; Hao, S.; Kirklin, S.; Morgan, D.; Wolverton, C. High-Throughput Computational Design of Cathode Coatings for Li-Ion Batteries. *Nat. Commun.* **2016**, *7* (1). https://doi.org/10.1038/ncomms13779.
112. Towns, J.; et al. XSEDE: Accelerating Scientific Discovery. *Comput. Sci. Eng.* **2014**, *16*, 62–74.

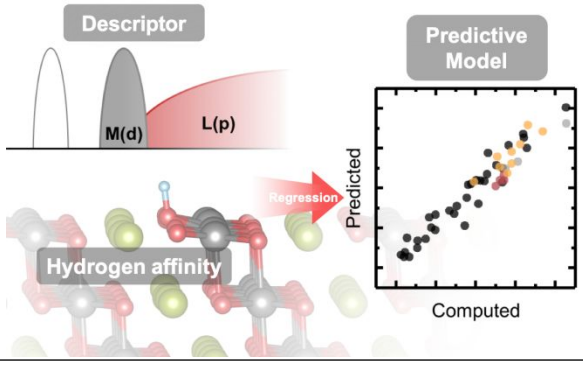
Descriptor
M(d)
L(p)
Predictive Model
Regression
Predicted
Computed
Hydrogen affinity